Estimating Vertical Motion Profile Shape within Tropical Weather States over the Oceans

ZACHARY J. HANDLOS AND LARISSA E. BACK

University of Wisconsin–Madison, Madison, Wisconsin

(Manuscript received 3 October 2013, in final form 12 July 2014)

ABSTRACT

The vertical structure of tropical deep convection strongly influences interactions with larger-scale circulations and climate. This paper focuses on investigating this vertical structure and its relationship with mesoscale tropical weather states. The authors test the hypothesis that latent heating plus turbulent flux convergence varies (in space and time) in association with weather state type.

The authors estimate mean-state vertical motion profile shape and latent heating plus turbulent flux convergence for six weather states defined using cloud-top pressure and optical depth properties from the International Satellite Cloud Climatology Project (ISCCP) dataset. Assuming two modes of vertical motion profile variability, these modes are statistically extracted from reanalysis data using a principal component analysis. Using these modes and the relationship between vertical motion, the dry static energy budget, and mass continuity, the authors estimate vertical motion profile shape. In these estimates, the authors use Global Precipitation Climatology Project (GPCP) [and Tropical Rainfall Measuring Mission (TRMM) 3B42] precipitation and Quick Scatterometer (QuikSCAT) surface convergence data in the ITCZ region from 2001 to 2006. Finally, these profile shapes are categorized by weather state type and spatiotemporally averaged to generate mean-state vertical motion profiles and latent heating plus turbulent flux convergence.

The authors find that vertical motion profile shape varies by weather state. The isolated systems convective regime exhibits more ''bottom heaviness'' than the other convectively active regimes, with maximum upward vertical motion occurring in the lower troposphere rather than the middle to upper troposphere. The variability observed does not coincide with the conventional profile variability based on stratiform rain fraction.

1. Introduction

Understanding the relationship between tropical convection and the large-scale atmospheric circulation is vital to improving our understanding of tropical weather and climate. Early studies of this relationship showed that imposing anomalous heat sources in the equatorial region induce an atmospheric circulation response (Matsuno 1966; Gill 1980). Latent heating variability, both in the horizontal and vertical, plays a significant role in this relationship. In this work, we examine vertical motion profiles in various tropical weather states.

In the atmosphere, rising air parcels (theoretical packets of air) cool less rapidly with height than they would if they were dry because of the condensation of water vapor. These buoyant updrafts, making up only a small fraction of the area of a cloud field, induce subsidence around them, rapidly warming the environment near clouds (Bretherton and Smolarkiewicz 1989). The combination of the condensational processes and the turbulent circulations associated with these pulses make up part of the apparent heating of the tropical atmosphere (Yanai et al. 1973), of which latent heating is a significant component (Tao et al. 2006).

Vertical profiles of latent heating (the distribution of latent heating in the vertical) are related to the vertical distribution of condensation, evaporation, melting, and freezing, as well as where clouds and precipitation develop. We can use these profiles to gain insight into global energy and moisture budgets. Latent heating profiles are also closely related to vertical profiles of vertical motion; such profiles provide information about the export of moist static energy and the gross moist stability of the atmosphere (Neelin and Held 1987; Back and Bretherton 2006; Raymond et al. 2009; Masunaga and L'Ecuyer 2014), and vertical motion profiles are also related to ensembles of deep convective clouds and their radiative effects (Bretherton and Hartmann 2009). Recent work also

Corresponding author address: Zachary J. Handlos, University of Wisconsin–Madison, 1225 West Dayton St., Madison, WI 53706. E-mail: handlos@wisc.edu

DOI: 10.1175/JCLI-D-13-00602.1

suggests that the amount of ''bottom heaviness'' associated with heating profiles (which we investigate here) is correlated to climate sensitivity in climate model simulations (Sherwood et al. 2014), and more accurate retrievals will reduce error associated with this sensitivity. Thus, in order to understand the relationship between convection and the large-scale circulation, it is important to understand vertical latent heating profile variability.

Earlier studies considering the large-scale atmospheric response to heating in the tropics assume a single and spatially uniform mode of heating (Gill 1980; Geisler 1981; DeMaria 1985). Studies such as Hartmann et al. (1984), Wu et al. (2000), and Schumacher et al. (2004) showed the significance of considering variability in the shape of latent heating profiles. More recent studies have shown that substantial geographic variability exists with respect to these heating profiles (Trenberth et al. 2000; Zhang et al. 2004; Back and Bretherton 2006), which should be considered when investigating the convection–large-scale circulation relationship.

Vertical profiles of latent heating are difficult to retrieve. The earliest methods of retrieving apparent heating by cumulus convection, of which latent heating is the most variable component, involved the direct calculation of apparent heating from sounding wind and temperature data using the dry static energy budget (Yanai et al. 1973). This method, still used during field campaigns, requires calculating vertical motion from a sounding array. With the increase in satellite technology and observation over the past few decades, we are now able to collect and analyze observational data in regions where observations were once limited. A variety of algorithms have been constructed in order to estimate latent heating profiles from satellite data.

For example, several latent heating profile retrieval algorithms were derived using data from the Tropical Rainfall Measuring Mission (TRMM) satellite, as one primary goal of TRMM was to improve latent heating profile retrieval (Tao et al. 2006). Four such algorithms are the Convective-Stratiform Heating (CSH) product (Tao et al. 1993, 2001, 2006), the Spectral Latent Heating (SLH) product (Shige et al. 2004, 2007, 2008, 2009), the Precipitation Radar Heating (PRH) product (Kodama et al. 2009), and the Training (TRAIN) algorithm (Grecu and Olson 2006; Grecu et al. 2009). These algorithms consider surface precipitation, percent stratiform rain fraction, and, for the PRH product, vertical profiles of reflectivity.

Hagos et al. (2010) investigates apparent heating profiles (where latent heating is the most dominant component) over the tropical ITCZ derived from different datasets and algorithms (Fig. 3 in their study). It is clear that the profile estimates differ significantly between the various observational, model, and reanalysis datasets, showing that these retrievals are not straightforward. Along with this, several other studies (Zuluaga et al. 2010; Jiang et al. 2011; Ling and Zhang 2011) suggest that shallow heating is particularly difficult to retrieve.

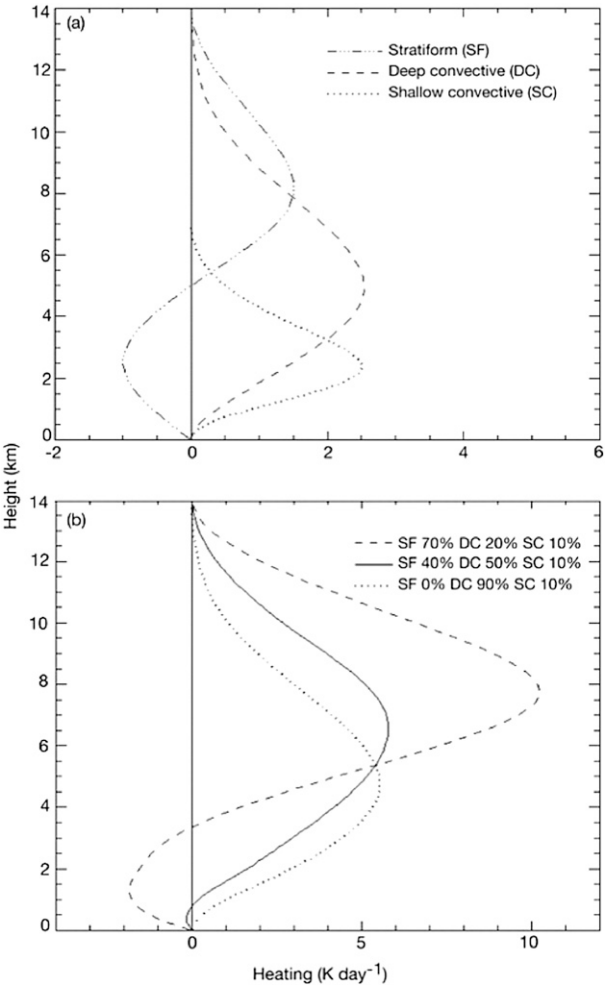

FIG. 1. From Schumacher et al. (2004): (top) Idealized latent heating profile modes; (bottom) idealized latent heating profiles for various percent stratiform rain fraction cases (shallow convective rain fraction held constant).

One view on latent heating profile variability is that the profiles are tied to the fraction of stratiform rain amount at a particular point (Zipser 1977; Houze and Betts 1981; Houze 1982, 1989, 1997, 2004; Mapes and Houze 1995; Schumacher et al. 2004; Jakob and Schumacher 2008; Johnson et al. 2013, manuscript submitted to *Meteor. Monogr.*). A conceptual model of this latent heating profile classification is shown in Fig. 1, adapted from Schumacher et al. (2004). Times with a high percentage of stratiform rain fraction are associated with a more top-heavy profile shape, where the maximum magnitude of latent heating occurs in the upper

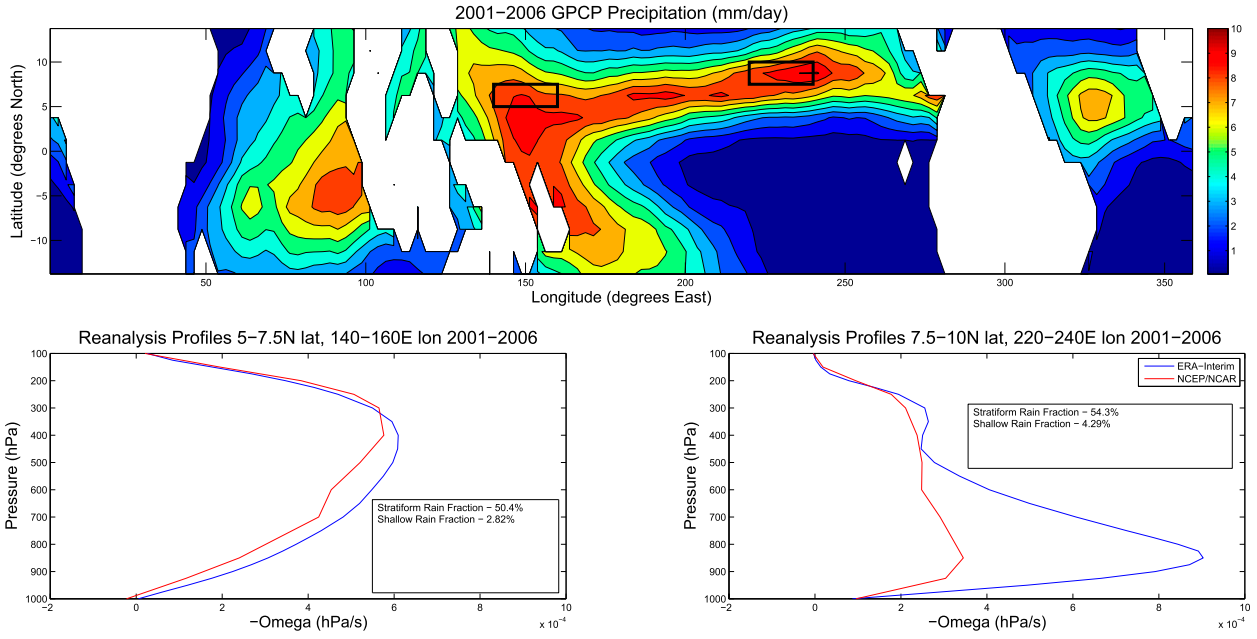

FIG. 2. Adapted from Back and Bretherton (2006, 2009b): Daily averaged (with 3-day running mean applied) 2001–06 GPCP precipitation with black boxes outlining the western and central-east Pacific regions of interest. Vertical motion profiles in the (bottom left) western Pacific and (bottom right) central-east Pacific regions investigated in Back and Bretherton (2006) for the years 2001–06. Mean-state stratiform and shallow rain fraction amounts for each region computed from the TRMM 3A25 product are also shown.

troposphere. Times with a high percentage of convective rain fraction (or low stratiform rain fraction) are associated with a more bottom-heavy profile shape, though convective heating profiles may vary geographically and/or temporally (Houze 1989).

Research by Back and Bretherton (2006) hints that stratiform rain fraction, as observed by radar echoes, may not be the most useful way to understand geographic variability in vertical motion profiles. The authors investigate vertical motion profiles within two regions along the tropical ITCZ; Fig. 2 in our study reproduces vertical motion profiles in the regions from Fig. 3 of Back and Bretherton (2006). In the western Pacific region (5°–7.5°N, 140°–160°E), the reanalyses exhibit a top-heavy profile, while in the central-eastern Pacific region (7.5°–10°N, 120°–140°W), a bottom-heavy profile is simulated. Back and Bretherton (2006) find that AGCMs forced by climatologically varying SSTs consistently have these vertical motion profile characteristics in these regions, and the ratio of 6-km to 2-km reflectivity also supports this picture (see Fig. S1 of Back and Bretherton 2006).

Furthermore, we find using TRMM 3A25 monthly data that the west Pacific region exhibits a slightly lower stratiform rain fraction (~50.4%) compared to the central-east Pacific region (~54.3%). The bottom-heavy central-eastern Pacific profiles are associated with a slightly higher shallow rain fraction (~4.29%) compared to the western Pacific (~2.82%). However, the difference in shallow rain fraction is only a few percent. These findings, along with our Fig. 2, suggest that stratiform rain fraction as observed by radar may not be a good way to retrieve geographic variability in latent heating profiles.

Houze (1989) documents that convective profiles may vary within varying mesoscale convective system environments within field campaign data, which may play a role in the seeming contradiction we observe. Shige et al. (2007) show that total heating profile "top heaviness" is not always directly related to the stratiform rain fraction (in comparing profiles between different geographic regions). This also differs from what one may expect from using stratiform rain fraction for profile retrieval.

The central-east Pacific region has about twice as much surface convergence as the western Pacific region, but both regions have similar amounts of rainfall. This is consistent with our vertical motion profile findings, since more bottom-heavy vertical motion profiles are associated with stronger lower-tropospheric convergence in the ITCZ given similar amounts of rainfall; this is discussed in Back and Bretherton (2009b). Our goal is to compare the bottom heaviness of vertical motion profiles spatiotemporally using satellite observations rather than reanalysis or model data.

We use an innovative methodology to estimate vertical motion profile shape (bottom heaviness) for six

TABLE 1. Description of the six weather states summarized from Rossow et al. (2005, 2013).

	Weather state description
Vigorous convective	Most vigorous deep convection with mesoscale anvils; deep convection covers largest area
Thick cirrus	Less vigorous deep convection with mesoscale anvil clouds (i.e., thick cirrus outflow)
Isolated systems	Low cloud tops with medium optical thickness mixed with deep convective clouds with higher cloud tops; some cumulus congestus
Thin cirrus	Thin cirrus outflow likely from distant convection or from other nonconvective atmospheric features
Mixed trade shallow cumulus	Mixed trade shallow cumulus (with some thin cirrus mixed in as well)
Marine stratus	Stratus, stratocumulus clouds (low but thicker nonconvective clouds)

tropical mesoscale weather states that occur over the tropical oceans, testing the hypothesis that latent heating (plus associated turbulent dry static energy flux convergence) profile shapes vary, in space and time, in association with weather state type. Our methodology is inspired by the weak temperature gradient approximation (Sobel and Bretherton 2000). We assume that apparent heating (Yanai et al. 1973) is large, compared to changes in the temperature profile over longer-than-diurnal time scales, and that it is predominantly balanced by adiabatic cooling associated with large-scale vertical motion. This assumption allows us to estimate vertical motion profiles from observational data (using reanalysis data only for deriving our basis functions). We also show that stratiform rain fraction (and shallow rain fraction) as observed by TRMM Precipitation Radar (PR) cannot explain the variations in bottom heaviness observed between weather states.

In this study, weather state type refers to any of six weather states or cloud regimes described in Rossow et al. (2005, 2013). To define these weather states, the authors created two-dimensional histograms of cloud-top pressure and optical depth data from the International Satellite Cloud Climatology Project (ISCCP; see Rossow and Schiffer 1999 for details) for each spatiotemporal grid point considered and then performed a clustering analysis on this data within the ITCZ region. The dataset assigns a value between 0 and 6 for each point, where values 1–6 represent a particular weather state (Table 1), and 0 represents clear sky (we neglect these points in our study). ISCCP has been used in previous studies for defining convectively active cloud systems (Machado and Rossow 1993; Jakob and Tselioudis 2003), but we use the most recent weather states from studies such as Rossow et al. (2005, 2013). Furthermore, while these weather states were initially classified based on cloud-top properties only, a recent study by Tselioudis et al. (2013) shows that ISCCP weather states have a unique vertical cloud layer structure to them as well.

Histograms of optical thickness and cloud-top height for each weather state are shown in Fig. 3. Table 1 provides a detailed description of each weather state along with their short-hand names used in later sections of this study. The top row (Fig. 3) shows the histogram pattern associated with the convectively active tropical mesoscale weather states. The top-left histogram is associated with the most vigorous deep convective systems with mesoscale anvils, covering the largest area out of all of the convectively active weather states. The top-middle panel is associated with less vigorous deep convective systems (less area coverage compared to the first weather state) with mesoscale anvils (thick cirrus outflow); the less vigorous deep convection is closely associated in space and time with the most vigorous deep convective weather state (Rossow et al. 2005, 2013). The third convectively active regime (top-right panel) is comprised of isolated, disorganized convection with some cumulus congestus and lower topped clouds. The convectively inactive regimes (bottom row of Fig. 3) consist of thin cirrus outflow that is not associated with convection, as well as mixed shallow cumulus and stratus with low cloud tops, and finally stratus clouds with some stratocumulus and thick but low cloud tops.

The goal of our study is to estimate vertical motion profile shape (bottom heaviness relative to other weather states) within each of these six weather states. We also wish to estimate latent heating plus convergence of turbulent heat fluxes (e.g., the apparent heating by convection). Section 2 briefly summarizes the various datasets used in this study. Section 3 shows the relationship between vertical motion, precipitation, and surface convergence. Section 4 describes our methodology, including the construction of vertical motion profile statistical modes of variability and a discussion on how to estimate vertical motion profile shape using these basis functions along with the relationships discussed in section 3. In section 5, we test our methodology. Section 6 shows the results from estimating vertical motion profile shape within the various ISCCP weather states and also addresses the validity of some of the key assumptions used in this study. Section 7 further discusses how stratiform rain fraction (and shallow rain fraction) is related to bottom heaviness in these weather states. Conclusions and potential future work are discussed in section 8.

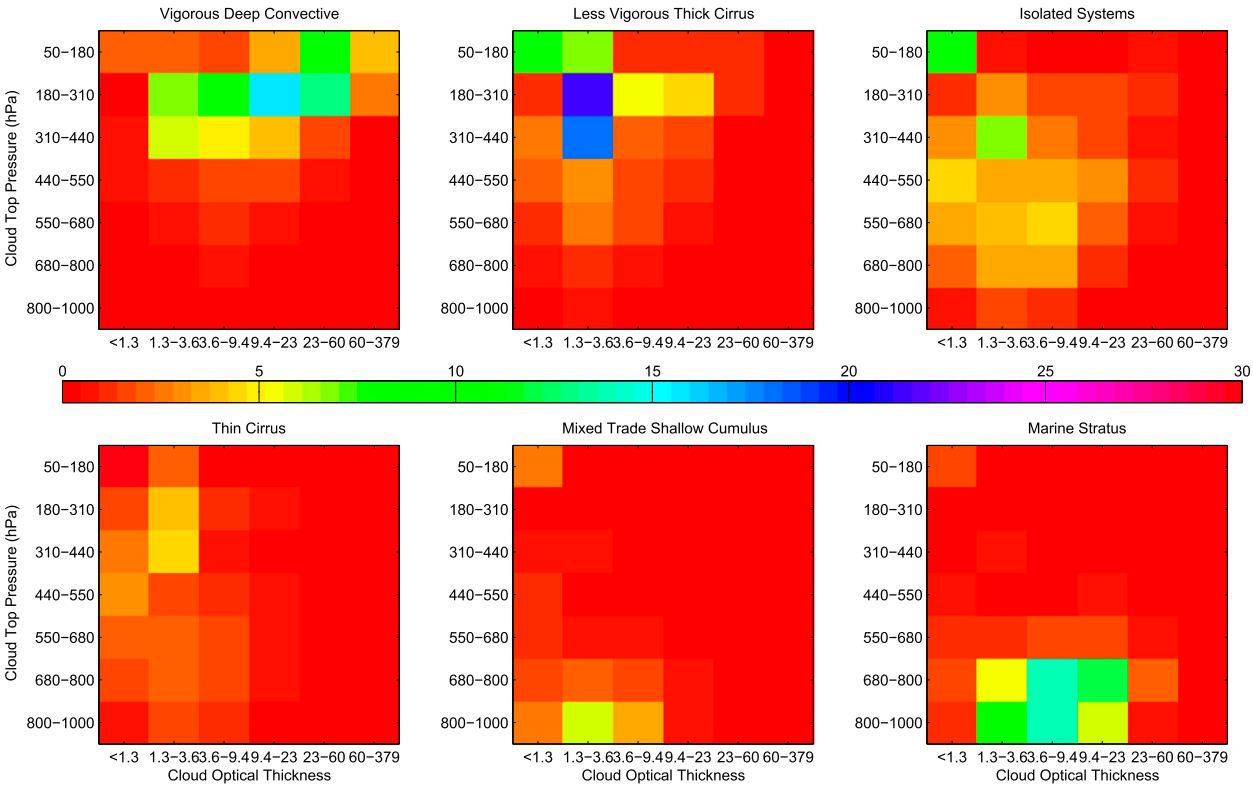

FIG. 3. Adapted from Rossow et al. (2005, 2013), two-dimensional histograms of cloud-top pressure (PC) and optical thickness (TAU) for each weather state. (top) The convectively active weather states are the (left) vigorous deep convective, (middle) lesser deep convective with thick cirrus, and (right) isolated systems weather states. (bottom) The convectively inactive weather states are the (left) thin cirrus, (middle) mixed trade shallow cumulus, and (right) marine stratus weather states. Colder colors indicate a higher frequency of occurrence.

2. Data

We summarize the datasets we use in this study in Table 2. To construct vertical motion profile basis functions (see section 4), we use the Interim European Centre for Medium-Range Weather Forecasts (ERA-Interim) (Dee et al. 2011) and National Centers for Environmental Prediction–National Center for Atmospheric Research (NCEP–NCAR) Reanalysis-1, as well as the Tropical Global Ocean Atmosphere Coupled Ocean Atmosphere Response Experiment (TOGA COARE; Webster and Lukas 1992; Ciesielski et al. 2003) field experiment [using data from the intensive observation period (IOP) Intensive Flux Array (IFA)]. To estimate vertical motion profiles, we combine these basis functions with observed precipitation data from the Global

TABLE 2. Summary of all datasets used. Note that the left of the two numbers in any given cell represents the original resolution, and the right value represents the resolution to which we convert the data.

	Horizontal resolution	Vertical (pressure) levels	Temporal resolution
ERA-Interim	~0.7°–2.5°	27	6-hourly to 3-day
NCEP	2.5°	12	Daily to 3-day
TOGA COARE	—	37	3-hourly
ISCCP	2.5°	1	3-hourly to Daily
GPCP	1.0°–2.5°	1	Daily to 3-day
QuikSCAT	0.25°–2.5°	1	3-day
Blended QuikSCAT/NCEP	0.25°–2.5°	1	Daily to 3-day
TRMM 2A23	2.5°	—	Instantaneous to daily
TRMM 2A25	2.5°	—	Instantaneous to daily
TRMM 3B42	0.25°–2.5°	—	Daily to 3-day
NEWS	2.5°	—	Instantaneous to 3-day

Precipitation Climatology Project (GPCP; Huffman et al. 2001) One-Degree Daily (1DD) dataset and surface wind data from both the Quick Scatterometer (QuikSCAT) surface wind and blended QuikSCAT/NCEP datasets (Milliff et al. 2004; Lungu 2006). Note that we did not consider space–time points in the QuikSCAT data that were marked as rain-flagged points, because such points may contain significant errors in surface wind speed (discussed further in section 6). We also use the National Aeronautics and Space Administration (NASA) Energy and Water cycle Study (NEWS) version 1 Atmospheric Heating Product (L'Ecuyer and Stephens 2003, 2007; Grecu and Olson 2006; Grecu et al. 2009; L'Ecuyer and McGarragh 2010) to compute vertically integrated net radiative heating and use in our methodology, outlined in section 4. Finally, we use TRMM algorithms 2A23 and 2A25 data to estimate stratiform and shallow rain fraction in our analysis. For all reanalysis and observed datasets, we reduce the spatial resolution to 2.5° so that the resolution is consistent with the ISCCP dataset. We also reduce the temporal resolution of all datasets (minus ISCCP and TRMM 2A23 and 2A25) to a daily time scale with a 3-day running mean applied such that each day in each dataset is the center of the 3-day mean.

Note that the ISCCP weather state dataset is a 3-hourly dataset (Table 2) and only includes daytime observations; our analysis in subsequent sections does not apply to convective systems and nonconvective clouds that occur at night. We convert the temporal resolution to a daily time scale. We do this by only considering grid points where only one type of weather state occurs at a grid point throughout a 24-h calendar day. For example, if the vigorous deep convective weather state occurs at a point for every non-clear sky 3-hourly observation on a particular calendar day, we construct a ω-profile for this point using daily average magnitudes of precipitation and surface convergence data for that grid point containing this weather state. If a second type of weather state occurs during this observational period (i.e., any of the other weather states), then the grid point is discarded. From this, our sample size for each weather state is ~3% − 14% of the total number of samples from the original 3-hourly dataset (range depending on the weather state considered). Figure 4 shows the spatial distribution of the total number of samples used per weather state. While the percent of points used is low, the sample size for each weather state is still large enough to provide a very good estimate of the mean state vertical motion profile in each weather state.

We estimate vertical motion profiles for each weather state in section 6. We will estimate such profiles using the methodology explained in the next few sections.

3. Vertical motion profiles, surface convergence, and precipitation

a. Latent heating profiles and vertical motion profiles

We construct vertical motion profiles by considering the relationship between vertical motion ω, surface convergence, and precipitation. To describe the relationship between ω and precipitation, we consider the dry static energy budget. Dry static energy is defined as $s = c_pT + gz$, where c_p is the specific heat at constant pressure, T is temperature, g is the gravitational constant, and z is altitude. Dry static energy is roughly conserved for dry adiabatic processes but is not conserved for moist adiabatic or diabatic processes. The dry static energy budget equation can be written as follows:

$$\frac{\partial s}{\partial t} = -\left(u\frac{\partial s}{\partial x} + v\frac{\partial s}{\partial y} + \omega\frac{\partial s}{\partial p}\right) + L(c-e) + g\frac{\partial}{\partial p}(F^s_{\text{turb}} + F_{\text{rad}}) + S_h, \quad (1)$$

where u and v are the zonal and meridional wind, respectively, ω is vertical motion, L the latent heat of condensation, and c and e are condensation and evaporation, respectively. The value $\partial F^s_{\text{turb}}\,\partial p^{-1}$ represents the vertical convergence of the vertical eddy transport of sensible heat, and $\partial F_{\text{rad}}\,\partial p^{-1}$ represents radiative flux convergence. The last term, S_h, is a residual predominantly associated with ice processes, as well as any kinetic energy that is locally dissipated into heat.

In the ITCZ region, the most variable terms in Eq. (1) are the vertical advection of dry static energy and latent heating. This is because horizontal gradients of dry static energy are small because of the large Rossby radius of deformation and because latent heating is the most variable diabatic heating term. Radiative heating and turbulent fluxes are also variable though much less than latent heating. Therefore, the variability associated with vertical profiles of ω is closely related to the variability associated with vertical profiles of latent heating.

We vertically integrate each term in Eq. (1) via Eq. (2):

$$[\alpha] = \int_{p_0}^{p_t} \alpha\frac{dp}{g}, \quad (2)$$

where α is the quantity being vertically integrated, and p_0 and p_t represent the 1000- and 100-hPa pressure levels, respectively. We assume that on diurnal and longer time scales, $\partial s\,\partial t^{-1}$ is small (see Table 3) and that all precipitation falls out as liquid, and we neglect S_h. The vertically integrated s budget equation is then written as follows:

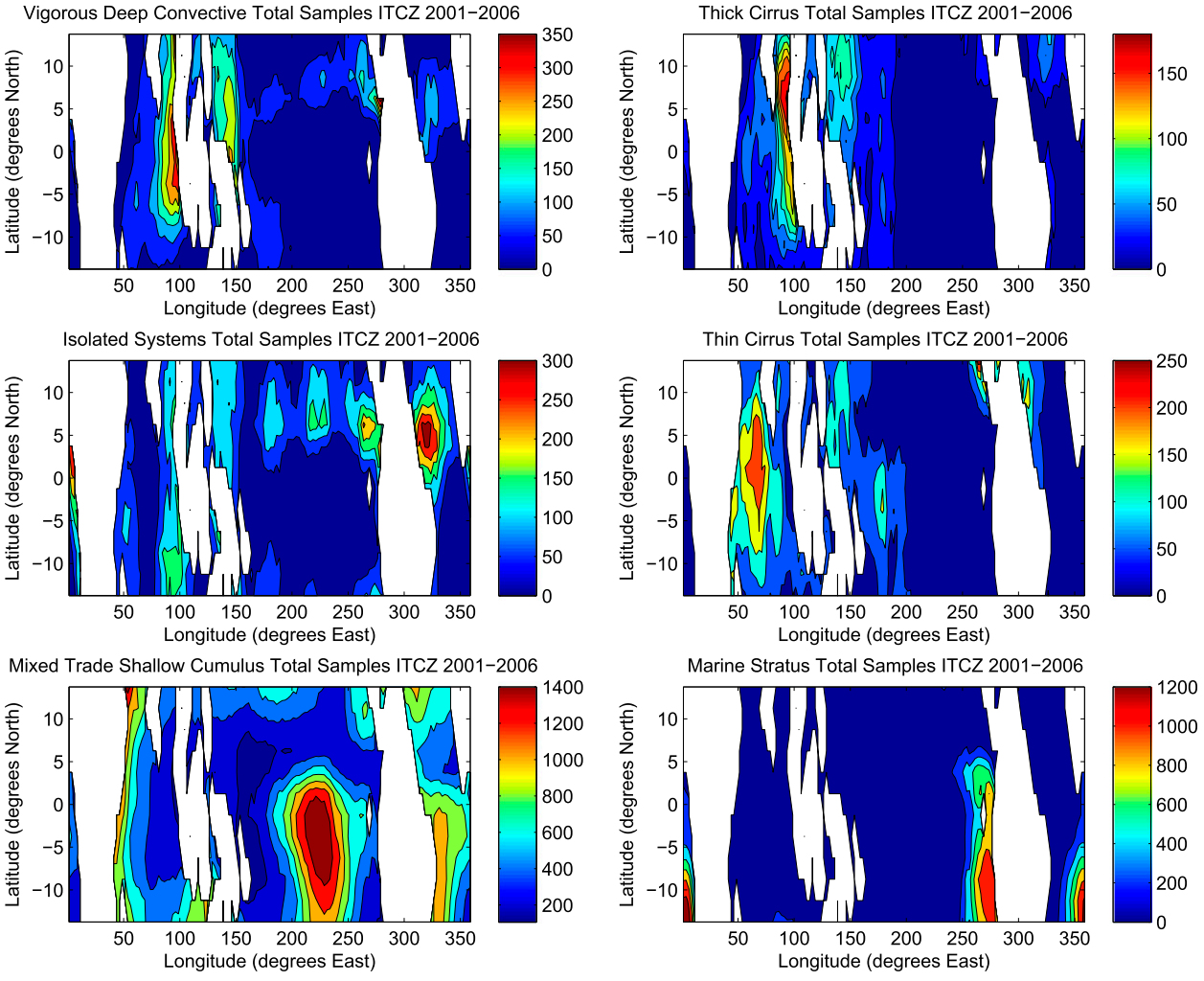

FIG. 4. Spatial distribution of the total number of daily weather state samples we use within the ITCZ from 2001 to 2006. Each daily weather state sample requires that only the same weather state occurs within a spatial grid box for a 24-h period (cannot have two or more weather state types in grid box over 24-h period).

$$\left[u\frac{\partial s}{\partial x}+v\frac{\partial s}{\partial y}\right]+\left[\omega\frac{\partial s}{\partial p}\right]=LP+\Delta F_{\mathrm{rad}}+F^{s}_{\mathrm{turb}}. \quad (3)$$

The terms on the left-hand side of Eq. (3) represent advection of s. The right-hand side terms (from left to right) represent vertically integrated latent heat release (where P is precipitation), divergence of radiative fluxes, and turbulent heat fluxes at the surface (we neglect turbulent fluxes at 100 hPa). Radiative cooling varies with the amount of convection occurring. However, the dominant balance in this equation is that diabatic heating variations due to latent heating are approximately balanced by adiabatic cooling associated with large-scale vertical motions.

We write the column-integrated version of this statement as

$$LP'\approx\left[\omega\frac{\partial s}{\partial p}\right], \quad (4)$$

where P' represents anomalous precipitation from the amount needed to balance radiative cooling plus surface fluxes of dry static energy (which are comparatively small). Dry static energy increases with decreasing pressure in the tropics. Hence, we can think of

TABLE 3. Root-mean-square error (W m^{-2}) associated with each neglected term in the dry static energy budget in this study. Note that for the TOGA COARE results, the tendency and advection terms were with respect to temperature, not dry static energy.

	ERA-Interim	NCEP–NCAR	TOGA COARE
$\left[\frac{\partial s}{\partial t}\right]$	13.0	13.2	20.3
$\left[u\frac{\partial s}{\partial x}+v\frac{\partial s}{\partial y}\right]$	32.5	29.0	17.8
F^{s}_{turb}	12.1	12.5	9.32
Total	35.2	40.2	27.5

anomalous latent heating as roughly proportional to the area under a curve showing ω as a function of pressure. Again, we can assume this dominant balance because of our steady state assumption and because the vertically integrated horizontal dry static energy advection and turbulent heat flux terms are small. The root-mean-square error over the tropical oceans associated with these neglected terms is shown in Table 3 (note that the tendency and horizontal advection terms from TOGA COARE are with respect to temperature, not dry static energy). This magnitude is small relative to LP' [and thus $\omega\ \partial s\ \partial p^{-1}$ by Eq. (4)], since the root-mean-square of LP' in the ITCZ region is approximately equivalent to $\sim 202\ \mathrm{W\ m^{-2}}$. Thus, our assumptions made with respect to the vertically integrated dry static energy budget are reasonable.

b. *Vertical motion profile, precipitation, and surface convergence relationship*

A conceptual model outlining the relationship between ω-profiles, precipitation, and surface convergence is shown in Fig. 5. Some arbitrary choices were made in this illustration in order to make clear to the reader visually how precipitation and surface convergence affect ω-profile shape; these profiles are not unique (i.e., not the only possible profile shapes that result in these relationships). The specific choices that we use in our quantitative analysis for estimating ω-profiles are described in the next section. This subsection qualitatively outlines the relationship between these variables.

The top panel shows the effects of precipitation rate given a fixed amount of surface convergence. The blue and red curves show ω-profiles for a low and high precipitation case, respectively. As shown in Eq. (4), the area under the $\omega(p)$ curve (i.e., area between $\omega = 0$ and the ω curve) is constrained by precipitation such that a ω–profile with more area under the $\omega(p)$ curve corresponds to more precipitation, and less area under the curve corresponds to less precipitation.

The bottom panel of Fig. 5 shows the effects of surface convergence for a fixed precipitation rate. The relationship between surface convergence and vertical motion we use is

$$-\left(\frac{\partial u}{\partial x}+\frac{\partial v}{\partial y}\right)=\frac{\partial \omega}{\partial p}=\frac{\omega_{pb}-\omega_{p0}}{p_b-p_0}, \tag{5}$$

where p_b and p_0 represent the pressure at 975 hPa (925 hPa for the NCEP–NCAR reanalysis) and 1000 hPa, respectively. Note that in subsequent sections, we use the term surface convergence to describe both 10-m horizontal convergence (retrieved by QuikSCAT) as well as 975–1000-hPa convergence. In the tropics, trade cumulus clouds mix the trade cumulus boundary layer well in the ITCZ region (Stevens et al. 2002; Back and Bretherton 2009a), so

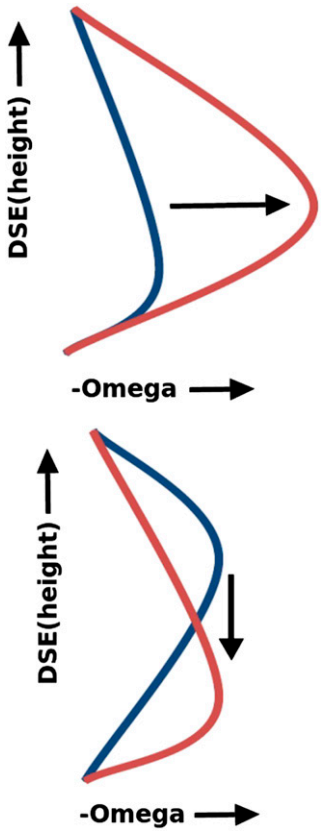

FIG. 5. Illustration of (top) the relationship between the shape of the vertical motion profile and the magnitude of precipitation, and (bottom) the relationship between the vertical motion profile shape and the magnitude of surface convergence.

convergence from 975 hPa to 1000 hPa is very well correlated with surface convergence. Thus, Eq. (5) is used to relate surface convergence to vertical motion throughout the rest of our study.

In the bottom panel of Fig. 5, note that the ω-profiles chosen for this panel are analogous to the west and central-east Pacific ω-profiles from Fig. 2, because these profiles nicely illustrate differences in profile shape for (approximately) fixed precipitation but differing magnitudes of surface convergence. The blue and red curves show ω-profiles for a low and high surface convergence scenario, respectively. Surface convergence acts as a constraint on the bottom heaviness of a ω-profile such that more surface convergence is associated with a more bottom-heavy ω-profile, and less surface convergence is associated with less bottom heaviness in a ω-profile (i.e., more middle- to top-heaviness), given rainfall is held fixed.

Based on the relationships shown in Fig. 5, we can use ω, precipitation, and surface convergence in order to estimate ω-profile shape. We do this by assuming two statistical modes of ω-profile variability in the tropics and using observed precipitation and surface convergence to

constrain the magnitude of these modes. Section 4 describes how we construct the modes of variability that we use as basis functions and also how we estimate ω-profiles.

Other modes of variability could be considered in order to further constrain (and improve) our ω-profile estimates. For example, a third mode of variability could be considered to improve the accuracy of our results. This would require a third constraint, such as an expression describing the ratio between 6-km and 2-km radar reflectivity. While we could have considered this ratio, the Precipitation Radar swath width is such that our estimates would only apply to a much smaller area. We also choose to assume only two modes of variability to maintain the simplicity of our methodology.

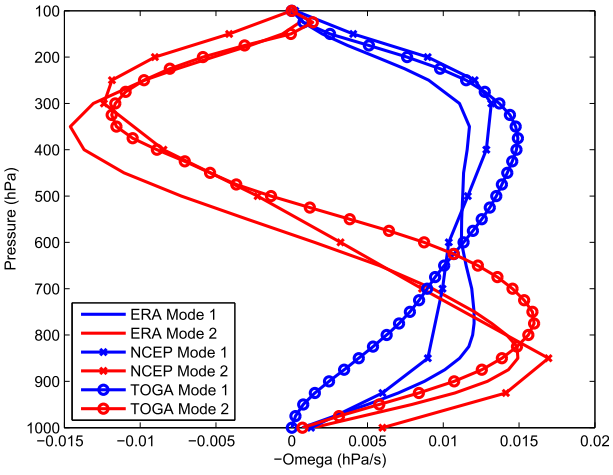

FIG. 6. Basis functions generated via principal component analysis of ERA-Interim (solid), NCEP–NCAR (solid with x symbols), and TOGA COARE (solid with circle symbols) vertical motion data from 2001–06.

4. Methodology

a. Generating basis functions

We will use our assumed two modes of ω-profile variability to define a vector space such that each vector within this vector space represents a possible ω-profile estimate. The vectors (ω-profiles) are linear combinations of two basis functions (statistical modes of variability), which we chose empirically (these basis functions are not related to the profiles in Fig. 5, which were arbitrarily chosen for illustration). The amount of influence that each basis function has on each space–time grid point that we consider is related to the amount of surface convergence and precipitation observed at that point. We wish to choose basis functions that can describe the maximum amount of observed variability in the profile of ω. We note that while Masunaga and L'Ecuyer (2014) similarly use basis functions to estimate large-scale vertical motions, we use basis functions statistically extracted from reanalysis data rather than idealized functions.

Ideally, observations would be used to generate basis functions, because the goal of our methodology is to be able to estimate observed ω-profiles using observational data rather than reanalysis. Unfortunately, since consistent observations of ω do not exist throughout the entire ITCZ domain we consider, reanalysis data serve as our best option for generating basis functions. We also try using TOGA COARE observations to construct basis functions, though we note that the TOGA COARE dataset does not include geographic variability; this may be a shortcoming of using these basis functions. We do not necessarily expect the latent heating profiles within each of the reanalysis datasets to be accurate in every location, though the ERA-Interim and NCEP–NCAR products do attempt to capture all physical processes that affect the shape and magnitude of latent heating profiles. This includes processes such as condensation, evaporation, melting, and freezing of water. Furthermore, using two reanalysis-generated sets of basis functions also allows us to examine the robustness of results to basis function choice. We also examine the sensitivity of our results to basis function choice in section 6.

To find basis functions, we perform a principal component analysis on daily ERA-Interim and NCEP–NCAR ω data in the tropical ITCZ region over ocean points only (15°S to 15°N latitude; all longitudes). We also perform this analysis on TOGA COARE ω data. The results of this analysis are shown in Fig. 6. For all three cases, the first mode, shown as blue profiles in Fig. 6, shows upward vertical motion throughout the middle and upper troposphere, while the second mode, shown as red curves, shows maximum upward vertical motion in the lower troposphere and maximum downward vertical motion in the upper troposphere.

The ERA-Interim and NCEP–NCAR modes are similar to the ω-profile variability shown in Back and Bretherton (2009b) and Zhang et al. (2010). However, the TOGA COARE first mode is more top heavy. This is likely due to a lack of geographic variability in the dataset. This leads to excessively bottom-heavy ω-profile estimates using our methodology (shown in section 6). The amount of variance explained by basis functions 1 and 2 is ~74.5% and 14.3% for the ERA-Interim basis functions, ~81.9% and 8.49% for NCEP–NCAR, and ~86.2% and 9.00% for TOGA COARE. These modes can be shown to be statistically distinct from each other using North's rule (North et al. 1982; not shown), even with the very conservative assumption that ~100 degrees of freedom exist in our analysis.

b. Constraining vertical motion profiles from precipitation and surface convergence observations

To estimate ω-profiles, (notation adapted from Back and Bretherton 2009b), we assume two modes of ω-profile variability:

$$\omega(x,y,t,p) = o_1(x,y,t)\Omega_1(p) + o_2(x,y,t)\Omega_2(p), \quad (6)$$

where Ω_1 and Ω_2 represent the basis functions, and o_1 and o_2 are the amplitudes of each basis function. Vertical motion at each grid point is thus a linear combination of the two basis functions constructed from our principal component analysis. The amplitudes describe how much influence each basis function has in shaping the ω-profile. To solve for the magnitudes of o_1 and o_2, we use observed precipitation and surface convergence in order to construct a closed system of equations with o_1 and o_2 as two unknown variables.

We can substitute Eq. (6) into Eq. (3) and neglect F^s_{turb} to get the following:

$$LP(x,y,t) = M_{s1}o_1(x,y,t) + M_{s2}o_2(x,y,t) - \Delta F_{\text{rad}}, \quad (7)$$

where we define M_{s1} and M_{s2} as

$$M_{si} = \int_{p_0}^{p_t} \Omega_i \frac{\partial s}{\partial p}\frac{dp}{g}; \quad i = 1,2. \quad (8)$$

Here, M_{s1} and M_{s2} represent the gross dry stability of modes 1 and 2, respectively. The gross dry stability is a measure of the amount of adiabatic cooling per unit amplitude of vertical motion (Yu et al. 1998; Back and Bretherton 2009b). Recall that the amount of precipitation is equal to the amount of vertically integrated latent heating due to condensation, which is in turn related to the amount of adiabatic cooling associated with large-scale vertical motion via Eq. (4). Thus, Eq. (7) is analogous to Eq. (4), though Eq. (7) is based only on the two most dominant statistical modes of ω-profile variability.

We also use surface convergence in order to constrain ω. We define the magnitude of surface convergence for each basis function as

$$c_i = \frac{\Delta\Omega_i(p)}{\Delta p}; \quad i = 1,2, \quad (9)$$

where Δ corresponds to the difference between the 975- and 1000-hPa levels. From this, surface convergence at any grid point is

$$\nabla \cdot \mathbf{u}(x,y,t) = o_1(x,y,t)c_1 + o_2(x,y,t)c_2, \quad (10)$$

where $\mathbf{u}$ is the 10-m wind. Since Eqs. (7) and (10) both contain o_1 and o_2 as unknowns, we can now solve for o_1 and o_2 and then use Eq. (6) to construct a ω-profile for each grid point. Equations (7) and (9) can be rearranged to derive the following values for o_1 and o_2, written in matrix form:

$$\begin{pmatrix} o_1 \\ o_2 \end{pmatrix} = \begin{pmatrix} M_{s1} & M_{s2} \\ c_1 & c_2 \end{pmatrix}^{-1} \begin{pmatrix} LP + \Delta F_{\text{rad}} \\ \nabla \cdot \mathbf{u} \end{pmatrix}. \quad (11)$$

The values M_{s1} and M_{s2} are calculated from a mean-state deep tropical dry static energy profile (i.e., space–time average over all longitudes from 15°S to 15°N latitude) and the basis functions, while c_1 and c_2 are calculated directly from the basis functions.

5. Testing our methodology

To test our methodology, we examine the same western Pacific (WP) and central-east Pacific (EP) regions as in Fig. 2. Figure 7 shows the reanalysis mean-state ω-profiles for each of these regions (solid lines, as in Fig. 2) using the ERA-Interim (top-left and top-right panels) and NCEP–NCAR (bottom-left) reanalyses. We first test whether truncating ω-profiles to two modes alters ω-profiles in these regions substantially. The panels of Fig. 7 have dashed lines, which show reanalysis profiles truncated to the two most dominant modes of ω-profile variability. Note that the top-right panel shows the truncated ERA-interim ω-profiles using basis functions constructed from the TOGA COARE dataset. The truncated reconstructions demonstrate that the two most dominant modes of ω are enough to describe variability in top heaviness seen in Fig. 2.

We then compare reanalysis ω-profiles to reconstructions, or ω-profiles we compute with our methodology using purely reanalysis precipitation (calculated as a residual), surface convergence, radiative cooling, the basis functions, and M_{si} as input into Eq. (11) for each region. We do this to test how accurately we can reconstruct ω-profiles from the reanalyses we use to construct our basis functions. Our methodology is linear; averaging surface convergence and precipitation before computing a profile produces the same results as computing ω-profiles for every point and then averaging them. Figure 7 shows these reconstructions for ERA-Interim data and basis functions (top left), ERA-Interim data with TOGA COARE basis functions (top right), NCEP–NCAR data and basis functions (bottom left), and TOGA COARE data using TOGA COARE, ERA-Interim, and NCEP–NCAR basis functions (bottom right).

The reconstructed profiles in each region using reanalysis basis functions look similar to the reanalysis ω-profiles, suggesting that our methodology has the

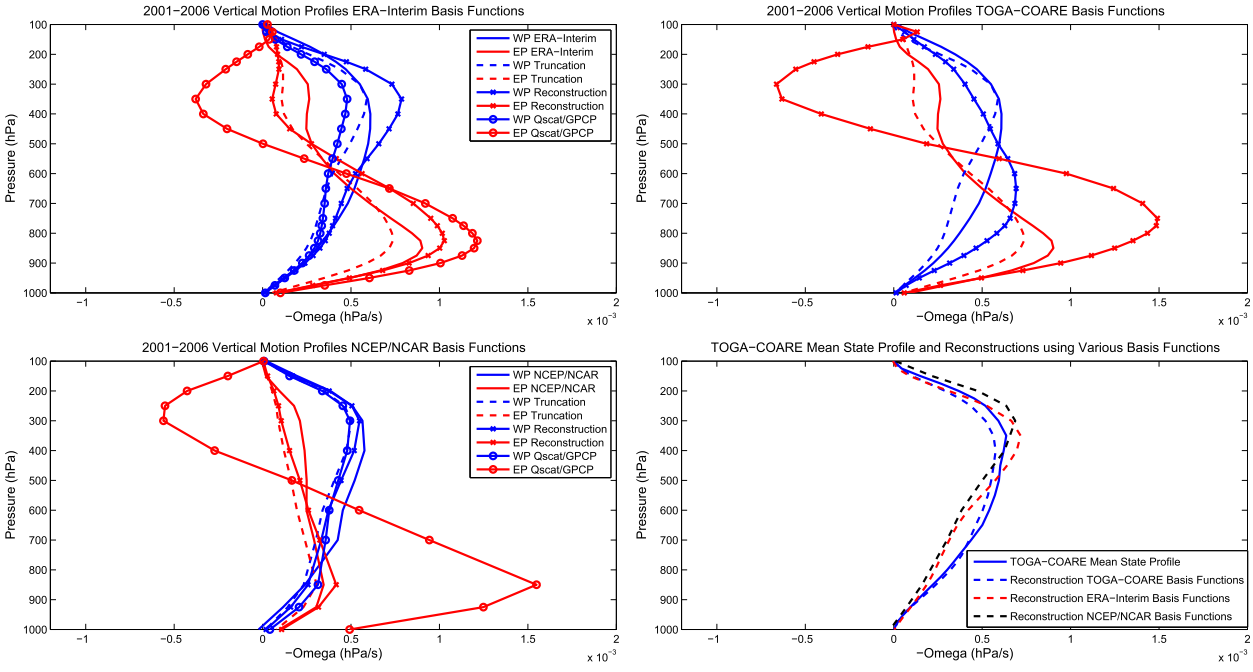

FIG. 7. The 2001–06 ω-profiles for the WP and EP regions defined in Fig. 2 using (top left) ERA-Interim, (bottom left) NCEP–NCAR, and (top right) TOGA COARE basis functions and reanalysis data. Blue lines represent various ω-profiles in the western Pacific ITCZ, and red lines the central-east Pacific ITCZ. (bottom right) Reconstructions of the mean state TOGA COARE ω-profile using the ERA-Interim, NCEP–NCAR, and TOGA COARE basis functions. See text for details.

potential to work reasonably well. The reconstructions using the NCEP–NCAR reanalysis data performed better at reconstructing NCEP–NCAR reanalysis profiles than did the corollary ERA-Interim reconstructions of ERA-Interim reanalysis profiles. This may suggest that there is something more complex in the ERA-Interim dataset compared to NCEP–NCAR, such that our methodology works better with NCEP data. However, the western Pacific reconstruction using ERA-interim data and TOGA COARE basis functions (top-right panel) has a more bottom-heavy ω-profile. It seems that using the TOGA COARE basis functions to estimate ω-profiles within the entire ITCZ region does not work because these basis functions are calculated from a dataset that only considers data in a limited region in the western Pacific. Thus, our study will not consider ω-profile estimates using TOGA COARE basis functions any further. Note that the TOGA COARE ω-profile reconstructions from both reanalysis basis functions (bottom-right panel of Fig. 7) are quite similar to the observed TOGA COARE ω-profile, suggesting that we can reasonably reconstruct ω–profiles despite our choice of basis functions in TOGA COARE.

Figure 7 also shows estimated ω-profiles, which were constructed using the reanalysis basis functions and observed GPCP precipitation and QuikSCAT surface convergence as well as observed radiative heating (from the NEWS dataset) rather than reanalysis data for these quantities. Although we find that our methods reproduce the essential features of the reanalysis profile shapes using reanalysis data, our estimations using observed precipitation and surface convergence data appear to be somewhat too bottom heavy. One reason why these estimations are more bottom heavy compared to the reanalysis data may be because the QuikSCAT-computed surface convergence values in the ITCZ are stronger in magnitude compared to the reanalysis-derived surface convergence values (not shown). As shown in Fig. 5, an increase in the magnitude of surface convergence at a given point is associated with more bottom heaviness.

Another reason for the more bottom-heavy ω-profile estimates from our methodology is because the GPCP precipitation dataset exhibits a lower magnitude of mean-state precipitation in the western Pacific region compared to the reanalysis residual precipitation. For example, Fig. 7 in our analysis shows that the ω-profile reconstructions versus the estimates using observed rainfall data are slightly more top heavy. In this case, the spatiotemporally averaged precipitation rate for the western Pacific is greater in the reanalysis dataset compared to the observed precipitation datasets ($\sim$11 mm day^{-1} of precipitation using ERA-Interim reanalysis versus $\sim$8.60 mm day^{-1} for GPCP, respectively). Splitting of our dataset into 6-month and yearly temporal bins also shows that the profile

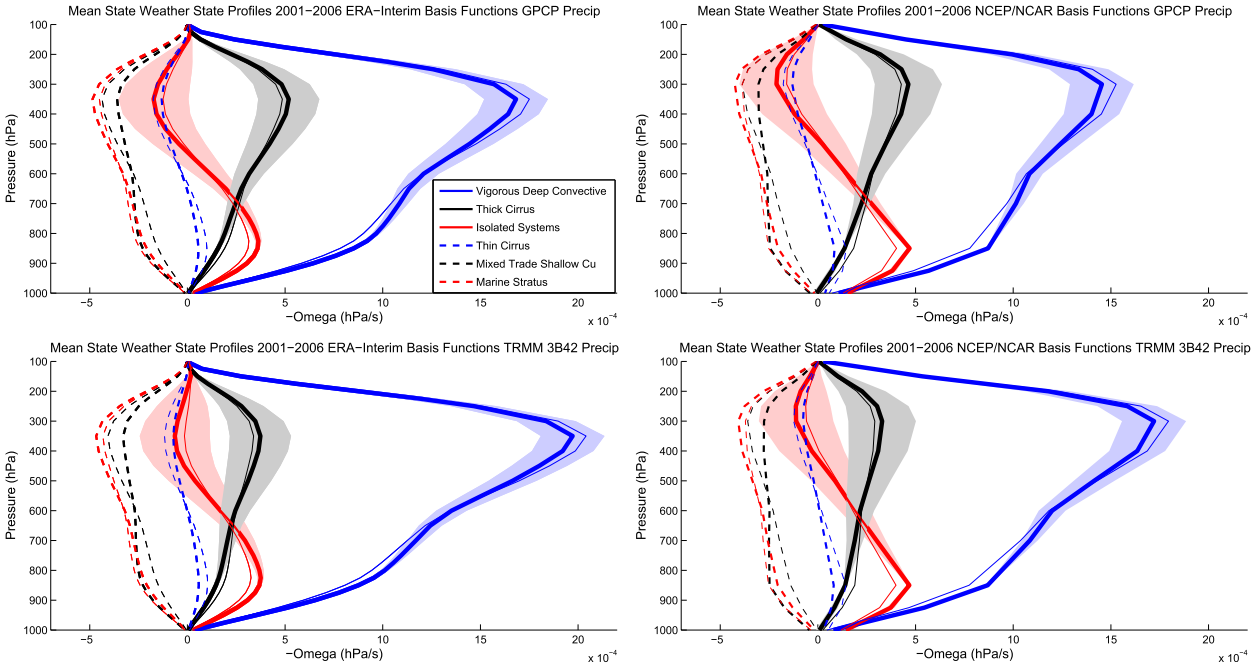

FIG. 8. The 2001–06 estimated mean-state vertical motion profile shapes for each ISCCP weather state using basis functions generated from the (left) ERA-Interim, and (right) NCEP–NCAR reanalysis basis functions. The convectively active weather state profile shapes are solid curves, and the convectively inactive weather states are dashed curves. The bold profiles with shading represent the mean-state profiles using GPCP/TRMM 3B42 precipitation and QuikSCAT-computed surface convergence as input into our methodology, with the shading representing the magntiude of the root-mean-square error associated with using Eq. (7). Thin profiles represent the mean-state profiles estimated using GPCP precipitation and QuikSCAT/NCEP blended surface convergence data. Mean-state profiles are estimated using (top) GPCP-observed precipitation and (bottom) TRMM 3B42 precipitation.

estimates using GPCP precipitation are more bottom heavy than the reconstructions (not shown). Revisiting Fig. 5, less precipitation along with more surface convergence (from the QuikSCAT surface convergence) is associated with more bottom heaviness. Thus, our ω-profile shape estimates can vary significantly depending on the precipitation and surface convergence datasets used.

Given the inherent limitations in observed vertical motion profile shape, and the uncertainties in the basis functions, we conclude that our methodology is working reasonably well. Therefore we use this methodology in the next section to estimate ω-profile shapes for each ISCCP tropical mesoscale weather state.

6. Mean-state vertical motion profiles within ISCCP tropical weather states

a. *Weather state vertical motion profiles*

To estimate the ISCCP weather state ω-profiles, we compute ω-profiles for all spatiotemporal points in the ITCZ region using our methodology from section 4. We then find all ω-profiles that correspond to each weather state event and compute the corresponding mean-state ω-profile. We do this analysis using the basis functions from reanalyses, and we use QuikSCAT observed surface convergence and GPCP and TRMM 3B42 observed precipitation. We do not use reanalysis precipitation or surface convergence because the reanalyses do not model precipitation associated with mesoscale convection well (Rossow et al. 2013) and because the goal of our methodology is to use observational data when possible. Finally, we only focus on grid points where a weather state occurs consistently throughout a 24-h period (discussed in section 2).

Vertical motion profiles for each weather state are plotted in Fig. 8. The left-side panels show the estimated ω-profiles using the ERA-Interim basis functions, and the right-side panels show profiles estimated using the NCEP–NCAR basis functions. The top panels use GPCP observational precipitation in these estimations, while the bottom panels use TRMM 3B42 precipitation.

Figure 8 shows that each weather state contains a unique ω-profile shape. The vigorous deep convective and less vigorous convective regime (thick cirrus outflow), which again are associated with each other closely in space and time, both exhibit a top-heavy ω-profile. Both the magnitude of surface convergence and precipitation for the less vigorous regime with thick cirrus is

significantly less than the vigorous convective regime, and thus less area between the profile and $\omega = 0$ is present in the thick cirrus case.

Unlike the two most vigorous convectively active weather states discussed above, the isolated systems weather state, associated with disorganized convection (Rossow et al. 2013) exhibits a bottom-heavy ω-profile shape (Fig. 8). This weather state has a higher magnitude of surface convergence in the mean state compared to the thick cirrus weather state but not as much surface convergence as the vigorous deep convective weather state. The isolated systems weather state is the only convectively active weather state that is significantly bottom heavy. Note that the thick cirrus weather state occurs frequently in the western Pacific region, and the isolated systems weather state occurs frequently in the central-east Pacific region (Fig. 2).

The mixed trade shallow cumulus and marine stratus weather states exhibit profiles containing downward vertical motion throughout the troposphere. The thin cirrus weather state exhibits minimal upward vertical motion because the mean precipitation associated with this weather state is offset by radiative cooling. The mean state profiles for these three convectively inactive weather states is expected since these weather states are not heavily precipitating. In these cases, warming by precipitation formation is less than radiative cooling, and downward vertical motion is required to help balance radiative cooling.

Our ω-profile estimates are qualitatively similar to those simulated within the Modern-Era Retrospective Analysis for Research and Application (MERRA) reanalysis dataset shown in Stachnik (2013) (not shown). Considering only the convectively active weather states, their WS3 is more bottom heavy than WS1 and WS2, similar to our results in our Fig. 8. Similarly, both their and our study show that the thick cirrus (WS2) regime is relatively more top heavy than the most vigorous convective weather state (WS1).

b. Sensitivity to basis function choice

Figure 9 shows mean-state weather state ω-profiles (bottom panel) using two sets of idealized basis functions (top panel) chosen to examine the sensitivity of our results to basis function choice. The isolated systems weather state still exhibits more bottom heaviness than the other convectively active weather state ω-profiles, and the less vigorous deep convection with mesoscale anvils (thick cirrus outflow) weather state is still more top heavy than the vigorous deep convective weather state. Figure 9 thus suggests that the bottom heaviness of the isolated systems weather state and the top heaviness of the thick cirrus weather state, relative to the other convectively active weather states, is likely a function of the mean-state precipitation and surface convergence, which come from observational data, rather than the basis functions chosen.

c. Latent heating profiles

Figure 10 shows mean weather state profiles of latent heating plus convergence of dry static energy due to turbulent fluxes [$L(c - e)$ and $g(\partial/\partial p)(F^s_{\text{turb}})$ terms in Eq. (1)], retrieved using ERA-interim basis functions and GPCP precipitation. This is the component of apparent heating directly due to convection (moist and dry), not including associated radiative effects. As in Figs. 8 and 9, the isolated systems weather state is most bottom heavy, and the less vigorous convective regime with thick cirrus outflow is more top heavy than the vigorous deep convective weather state. The less vigorous regime with thick cirrus outflow is also more top heavy than the vigorous deep convective weather state, since it has less of a low-level peak vertical velocity compared to the upper level vertical velocity. These results are consistent with what we see using the NCEP basis functions or idealized basis functions and/or TRMM 3B42 precipitation in the retrieval. Hence, they are quite robust.

d. Error associated with mean-state profiles

1) Error due to neglected terms in dry static energy budget

We consider the error associated with neglected terms in the dry static energy budget by calculating the root-mean-square error (RMSE) associated with neglecting the horizontal advection of dry static energy terms, along with the dry static energy tendency and surface turbulent heat flux terms. The RMSE for each mean-state ω-profile is shown as shaded regions for each profile in the reanalysis cases (Fig. 8). The figure shows that the addition or subtraction of such terms does not change the shape of the profiles, nor does this significantly change the amount of area contained within the mean-state ω-profile curves. Thus, it appears that our use of a first-order vertically integrated dry static energy budget is reasonable.

2) QuikSCAT observations versus blended data

Recall that QuikSCAT rain-flagged data points are discarded in our analysis, because such points may be contaminated and provide potentially inaccurate wind information. A downside to neglecting these points in our analysis is that many of the convectively active weather states are associated with higher amounts of precipitation, and thus, we lose some information we

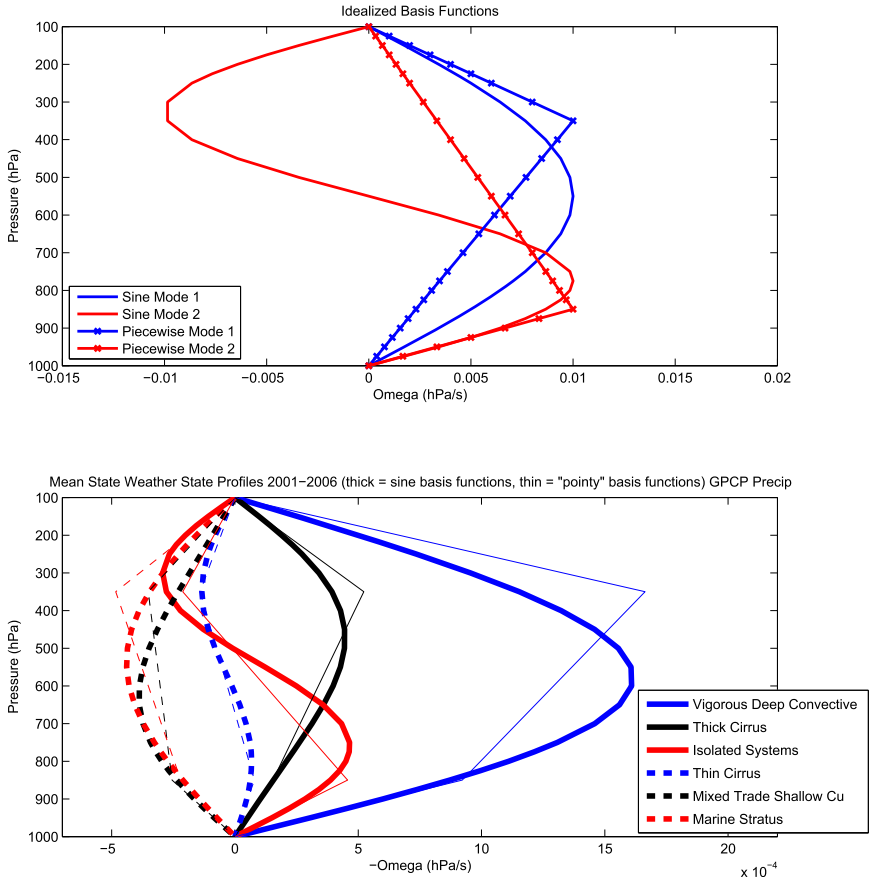

FIG. 9. As in Fig. 8, but mean-state weather state ω-profiles are estimated using two sets of idealized basis functions. (top) The two sets of basis functions used to estimate the ω-profiles. (bottom) The ω-profile estimates using GPCP precipitation. In (bottom), the thick lines represent the ω-profile estimates using the sine basis functions, and the thin lines represent profile estimates using the piecewise function basis functions.

could use in constructing the weather state ω-profiles. One way to alleviate such an issue is to blend the data with high-resolution reanalysis data. This was done in the construction of the QuikSCAT/NCEP Blended Ocean Winds dataset by Milliff et al. (2004). In this product, any rain-flagged points not considered in our previous analysis are now substituted with reanalysis data, and we can now consider such points in our analysis.

Figure 8 also shows mean-state ω-profiles for each weather state using GPCP precipitation and blended QuikSCAT/NCEP surface convergence in the top panels and TRMM 3B42 precipitation and the blended surface convergence data in the bottom panels (rather than purely QuikSCAT-computed surface convergence data). These ω-profiles are shown as thin-line profiles in each figure. The profiles are very similar to those estimated using QuikSCAT-only surface convergence. While the mixed trade shallow cumulus weather state does differ between the blended and pure QuikSCAT cases, the profiles still exhibit divergence as expected. Physically, the fact that the mean-state ω-profiles estimated using the blended data do not differ from the estimates using the QuikSCAT surface convergence data is a result of surface convergence changing slowly in space. Therefore, our results appear robust whether we neglect rain-flagged points or input reanalysis-derived surface convergence data in these rain-flagged points.

e. *Variability of weather state profile results*

We asses the amount of precipitation and surface convergence variability for each weather state, providing insight about the amount of ω-profile variability for each regime. First, Table 4 shows the 95% confidence intervals (lower and upper bounds) associated with each mean-state ω-profile. These values were computed via statistical bootstrapping about the mean-state precipitation and surface convergence values associated with each weather state. Since the range of the

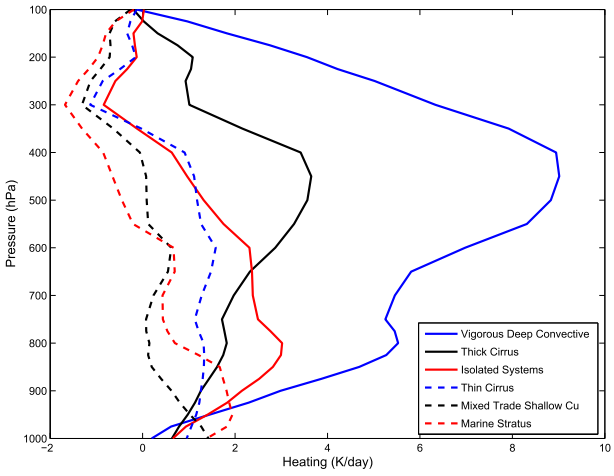

FIG. 10. As in Fig. 8, but profiles now represent mean-state weather state latent heating plus convergence of dry static energy due to turbulent fluxes; profiles were retrieved using ERA-interim basis functions and GPCP precipitation.

upper and lower limits is small, the table shows that the mean-state precipitation and surface convergence values for each weather state are very well constrained.

Figure 11 shows the amount of variability in observed precipitation and surface convergence for each weather state. The upper and lower limits of each bar represent the 25th and 75th percentile values associated with each variable, and the intersection represents the mean state for each weather state. The figure shows that there are significant differences between the 25th and 75th percentile values and the mean for both precipitation and surface convergence for each weather state. For both the convectively active (top panels) and inactive weather states (bottom panels), the range of precipitation and surface convergence values are about the same order of magnitude as the mean precipitation and surface convergence values themselves. It is not suprising that such variability exists with respect to the ω-profiles for each weather state, because there is significant variability resulting from the clustering analysis used to define these weather states. Table 4 and Fig. 11 show that while the mean state profiles are well constrained, the ω-profile variability for each weather state is large.

7. Stratiform rain fraction associated with each weather state

We estimate stratiform rain fraction for each weather state using the TRMM 2A25 PR product to further investigate the relationship between the shape of our ω-profile estimates and percent stratiform rain fraction associated with each profile. We bin the instantaneous stratiform and precipitation rain rate data into 2.5° daily averaged grid boxes and compare with the daily averaged 2.5° ISCCP weather state data. The vigorous deep convective weather state has the highest stratiform rain fraction at ~54.3%, while the other top-heavy weather state, thick cirrus, has only ~37.8%. The isolated systems weather state has a slightly higher stratiform rain fraction, ~41.1%, than thick cirrus. The thin cirrus, mixed trade shallow cumulus and marine stratus weather states have stratiform rain fractions of ~31.4%, ~20.2%, and ~29.3%, respectively.

These results are interesting, because differences in stratiform rain fraction do not seem to be predicting top heaviness. Despite having similar mean stratiform rain fraction percentages, the thick cirrus and isolated systems weather states exhibit significantly different mean-state ω-profile shapes (as shown in Fig. 8). This is consistent with our earlier discussion regarding the geographic location of the thick cirrus and isolated systems weather states, because these weather states are common in the western Pacific (lower stratiform rain fraction) and central-east Pacific (higher stratiform rain fraction) regions respectively (Fig. 4). As Fig. 12 shows, observed stratiform rain fraction in the eastern Pacific

TABLE 4. The 95% confidence limits on mean-state surface convergence and precipitation values for each weather state ω-profile along with 2001–06 mean-state TRMM algorithm 2A25 stratiform rain fraction and TRMM algorithm 2A23 shallow rain fraction for each ISCCP weather state.

	Vigorous convective	Thick cirrus	Isolated systems	Thin cirrus	Mixed trade shallow cumulus	Marine stratus
Surface convergence ($s^{-1} \times 10^{-5}$)	0.606–0.623	0.0946–0.111	0.299–0.310	0.0479–0.0611	−0.172 to −0.169	−0.149 to −0.143
GPCP precipitation (mm day^{-1})	20.2–20.3	7.32–7.46	4.79–4.85	3.02–3.10	0.555–0.564	0.462–0.478
TRMM 3B42 precipitation (mm day^{-1})	22.4–22.7	6.13–6.32	5.66–5.74	3.47–3.57	0.795–0.805	0.606–0.624
Stratiform rain fraction (%)	54.3	37.8	41.4	31.4	20.2	29.3
Shallow rain fraction (%)	0.947	4.51	4.64	6.64	17.5	20.2

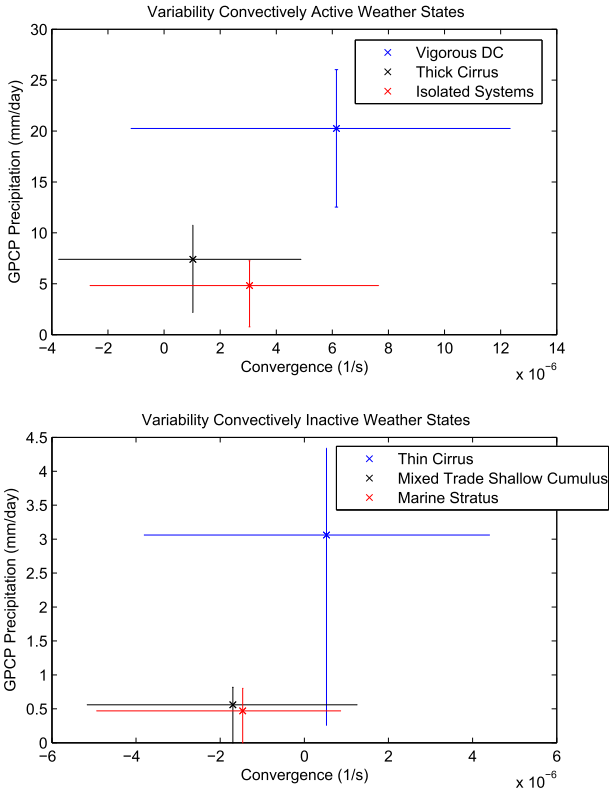

FIG. 11. Variability in QuikSCAT surface convergence and GPCP precipitation data within each weather state. The center point of each plot represents the mean-state surface convergence and precipitation values associated with each weather state. The error bar limits represent the 25th and 75th percentile limits. (top) The convectively active weather states and (bottom) the convectively inactive weather states.

is comparable (or higher in some regions) versus the western Pacific. Also, the vigorous deep convective and thick cirrus weather states both exhibit roughly equally top-heavy ω-profiles, with thick cirrus slightly more top heavy, despite a significantly larger stratiform rain fraction amount in the vigorous deep convective regime.

We also look at the shallow rain fraction percentage associated with each weather state using the TRMM 2A23 PR product to examine the idea illustrated in Fig. 1 that more shallow rain is associated with a more bottom-heavy latent heating profile. The shallow rain fraction is less than 1% in the vigorous deep convective weather state, but for the other two convectively active weather states, the shallow rain fraction is very similar (i.e., 4.51% for the thick cirrus versus 4.64% for the isolated systems weather state). Since the shallow rain fraction is not significantly larger in the isolated systems regime compared to the other convectively active regimes, shallow rain fraction does not seem to explain the bottom heaviness of the isolated systems ω-profile. These results suggest that combining stratiform and shallow rain fraction still does not seem to be predicting top heaviness of vertical motion or of latent heating (plus turbulent convergence of dry static energy fluxes) profiles.

Figure 13 shows the time-averaged geographic variability in the level of maximum upward vertical motion within each grid point in the ITCZ domain with respect to ω-profile estimates using ERA-Interim (top panel) and NCEP–NCAR (top-middle panel) reanalysis ω data, as well as ω-profiles estimated from observations using ERA-Interim (middle-bottom panel) and NCEP–NCAR (bottom panel) basis functions for the estimations, respectively. In all cases, a gradient exists across the rainy regions of the Pacific ITCZ such that the pressure of maximum upward vertical motion increases from the western to the eastern Pacific. Since Fig. 12 shows increasing stratiform rain fraction eastward in the Pacific, this means higher amounts of mean stratiform rain fraction are present in regions with more bottom-heavy vertical motion profiles. Figures 12 and 13 reinforce that using the stratiform rain fraction variability is not the best way to retrieve geographic variability in ω-profile and latent heating profile shape. This may be because geographic variability in stratiform and convective heating must be considered.

The majority of the rainiest regions along the ITCZ appear to consist of time-averaged ω-profiles that are

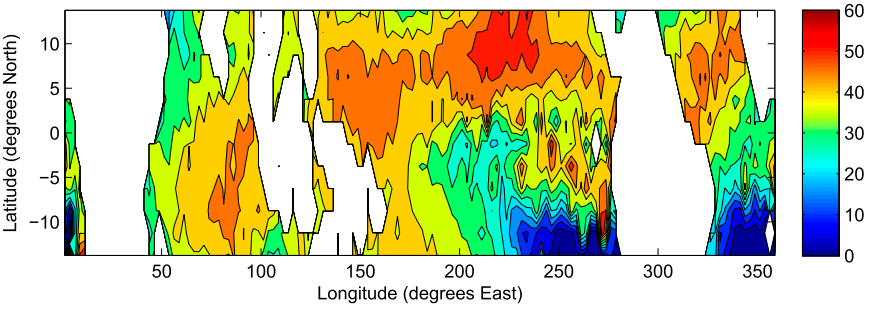

FIG. 12. Geographic distribution of the TRMM 2A25 computed 2001–06 mean stratiform rain fraction (%) across the ITCZ domain.

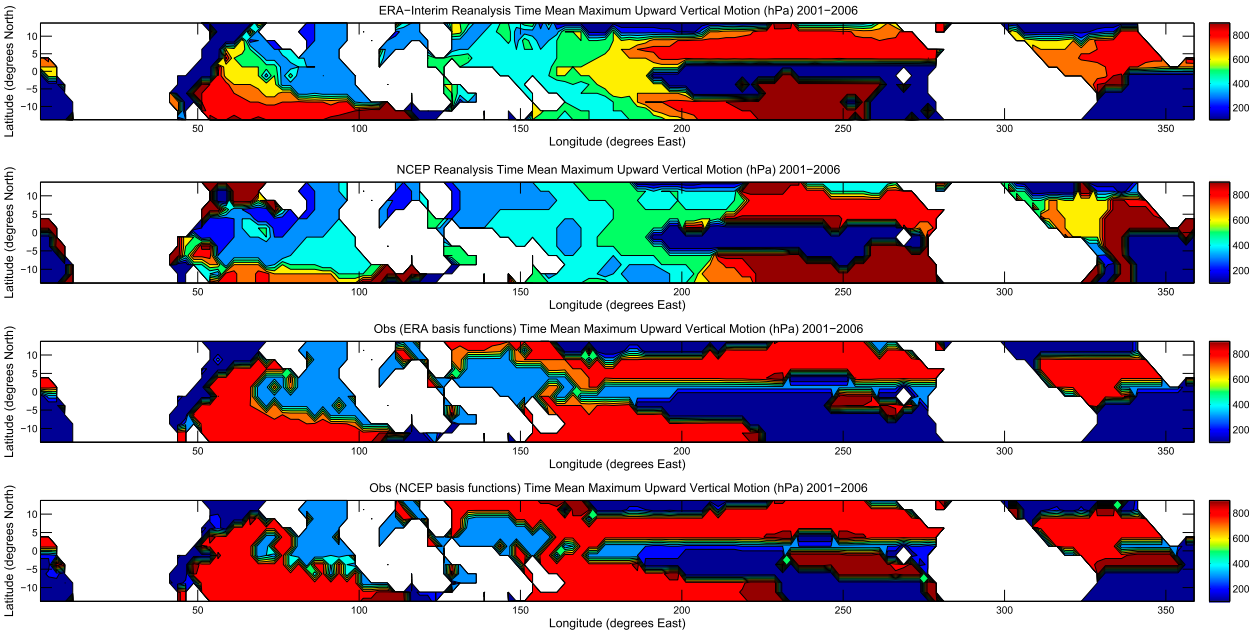

FIG. 13. Geographic distribution of the 2001–06 time-averaged maximum in upward vertical motion using the (top) ERA-Interim reanalysis ω data, (top middle) NCEP–NCAR reanalysis ω data, (middle bottom) estimated ω-profile data from observations using ERA-Interim-derived basis functions, and (bottom) estimated ω-profile data from observations using NCEP–NCAR-derived basis functions.

bottom heavy (or exhibit a maximum in upward vertical motion), except in the western Pacific, where time-averaged ω-profiles are top heavy. This is not the case in the ω data taken from the ERA-Interim and NCEP–NCAR reanalysis datasets, where several regions (i.e., the central Pacific) exhibit profiles that have a maximum in upward vertical motion in the middle troposphere. The use of only two basis functions may be a reason why our ω-profile estimates are too bottom heavy, or there may be other ways of generating basis functions (or correcting them) that would not have this issue. Other factors that likely play a role in our estimates being so bottom heavy are that surface convergence observations are larger than in reanalysis, precipitation patterns are different, and the energy budgets in the reanalysis do not close.

8. Conclusions

The goals of this study were to investigate the hypothesis that latent heating (plus turbulent flux convergence) profile shape varies (in space and time) in association with weather state type and to compare the bottom heaviness of different tropical weather states as defined by Rossow et al. (2005, 2013). We use reanalysis-constructed basis functions representing the two most dominant statistical modes of ω-profile variability (assuming that these two modes explain all ω-profile variability) and estimate the ω-profiles as a linear combination of these two modes based on observed GPCP precipitation, TRMM 3B42 precipitation, and QuikSCAT surface convergence data. We find that each weather state is associated with a unique mean-state ω-profile shape and convective-heating shape that is well constrained, despite the fact that significant profile variability is exhibited in profiles associated with each weather state. We examine the sensitivity of our results to basis function choice and conclude that the relative bottom heaviness in the isolated systems weather state as well as the top heaviness associated with the thick cirrus weather state relative to the more vigorous deep convective weather state is consistent regardless of basis function choice.

More basis functions could be used in order to further constrain (and improve) our ω-profile estimates. For example, a third mode of variability could be included to improve the accuracy of our results. A third basis function would require a third constraint, such as an expression describing the ratio between 6-km and 2-km radar reflectivity. However, the Precipitation Radar (PR) swath width is such that estimates would only apply to a much smaller area. We also choose to assume only two modes of variability to maintain the simplicity of our methodology. Future work may include investigation of additional constraints.

Our findings suggest that when considering geographic variability, higher stratiform rain fractions, as observed by radar, are not necessarily associated with

more elevated latent heating profiles. The isolated systems weather state is associated with a slightly higher stratiform rain fraction compared to thick cirrus despite the isolated systems mean-state ω-profile being much more bottom heavy. Time-averaged ω-profiles geographically vary such that regions of bottom-heavy ω-profiles are common in regions of higher stratiform rain fraction, and vice versa (Figs. 12 and 13).

Back and Bretherton (2009a,b) explored the controls on geographic variability in vertical motion profile top heaviness. They argued that the top heaviness of a profile is due to an interplay between the local SST gradients and the local SST compared to SST in other convecting regions of the tropics. The SST gradients contribute to convergence at low levels via the mechanism proposed by Lindzen and Nigam (1987), while the local SST, compared to the SST in other deeply convecting regions influences how deep convection develops. Regions with strong local SST gradients and cooler SST values are associated with more surface convergence but less deep tropospheric heating, leading to a more bottom-heavy ω-profile and the development of convection predominantly within the lower to middle troposphere. Regions with lesser magnitudes of SST gradients but warmer SSTs are associated with more top-heavy ω-profiles and deep convection.

The investigation of heating profiles from a cloud system perspective is scientifically interesting and worth pursuing, and interesting questions remain about how different cloud systems are related to vertical motion top heaviness. Controls on vertical motion bottom heaviness may be related to climate sensitivity (Sherwood et al. 2014), which suggests this is an important research area to pursue. Back and Bretherton (2009a,b) suggested that large-scale dynamical considerations can be used to understand much of the climatological geographic variability in ω-profiles over the tropical oceans. However, the relationship between this view and the cloud system perspective would be interesting to further clarify and explore.

Our methodology is designed to be applied to any investigation of vertical motion and apparent heating profiles in the tropical ITCZ region. We recommend that our methodology be compared with other vertical motion and apparent heating profile retrievals, including algorithms developed via TRMM, in order to improve overall latent heating profile retrievals. Our estimates could be used in models to simulate and further investigate the large-scale atmospheric response due to anomalous heating in the tropics. For example, our methodology may be useful in single-column modeling studies, where it is important to specify accurate nonzero ω-profiles when modeling a particular region in the tropics (Sobel and Bretherton 2000). The estimates would also be useful for investigating the evolution and variability of the vertical profile of ω and latent heating with respect to phenomena in the ITCZ region, such as the Madden–Jullian oscillation (Zhang et al. 2010; Jiang et al. 2011) and the El Niño–Southern Oscillation (ENSO; L'Ecuyer and Stephens 2007). Finally, we could also apply our estimates to studying moist static energy budgets, as in Masunaga and L'Ecuyer (2014), and the gross moist stability, which could be used to further understand feedbacks between the large-scale circulation and deep convection.

Acknowledgments. We thank Professor Tristan L'Ecuyer for providing access to the NEWS version 1 Atmospheric Heating Product dataset and useful feedback regarding this study. We would also like to thank Professor Gregory J. Tripoli for reading Zachary Handlos' M.S. thesis describing this work. Finally, we thank our anonymous reviewer as well as Professors Courtney Schumacher and Zhiming Kuang for their constructive criticism regarding our study. This research is supported by NASA Grant NNX12AL96G.

REFERENCES

Back, L. E., and C. S. Bretherton, 2006: Geographic variability in the export of moist static energy and vertical motion profiles in the tropical Pacific. *Geophys. Res. Lett.,* **33,** L17810, doi:10.1029/2006GL026672.

——, and ——, 2009a: On the relationship between SST gradients, boundary layer winds, and convergence over the tropical oceans. *J. Climate,* **22,** 4182–4196, doi:10.1175/2009JCLI2392.1.

——, and ——, 2009b: A simple model of climatological rainfall and vertical motion patterns over the tropical oceans. *J. Climate,* **22,** 6477–6497, doi:10.1175/2009JCLI2393.1.

Bretherton, C. S., and P. K. Smolarkiewicz, 1989: Gravity waves, compensating subsidence and detrainment around cumulus clouds. *J. Atmos. Sci.,* **46,** 740–759, doi:10.1175/1520-0469(1989)046<0740:GWCSAD>2.0.CO;2.

——, and D. L. Hartmann, 2009: Large-scale controls on cloudiness. *Clouds in the Perturbed Climate System: Their Relationship to Energy Balance, Atmospheric Dynamics, and Precipitation,* J. Heintzenberg and R. J. Charlson, Eds., MIT Press, 217–234.

Ciesielski, P. E., R. H. Johnson, P. T. Haertel, and J. Wang, 2003: Corrected TOGA COARE sounding humidity data: Impact on diagnosed properties of convection and climate over the warm pool. *J. Climate,* **16,** 2370–2384, doi:10.1175/2790.1.

Dee, D. P., and Coauthors, 2011: The ERA-Interim reanalysis: Configuration and performance of the data assimilation system. *Quart. J. Roy. Meteor. Soc.,* **137,** 553–597, doi:10.1002/qj.828.

DeMaria, M., 1985: Linear response of a stratified tropical atmosphere to convective forcing. *J. Atmos. Sci.,* **42,** 1944–1959, doi:10.1175/1520-0469(1985)042<1944:LROAST>2.0.CO;2.

Geisler, J. E., 1981: A linear model of the Walker circulation. *J. Atmos. Sci.,* **38,** 1390–1400, doi:10.1175/1520-0469(1981)038<1390:ALMOTW>2.0.CO;2.

Gill, A. E., 1980: Some simple solutions for heat-induced tropical circulation. *Quart. J. Roy. Meteor. Soc.,* **106,** 447–462, doi:10.1002/qj.49710644905.

Grecu, M., and W. S. Olson, 2006: Bayesian estimation of precipitation from satellite passive microwave observations using combined radar–radiometer retrievals. *J. Appl. Meteor. Climatol.,* **45,** 416–433, doi:10.1175/JAM2360.1.

——, ——, C.-L. Shie, T. S. L'Ecuyer, and W.-K. Tao, 2009: Combining satellite microwave radiometer and radar observations to estimate atmospheric heating profiles. *J. Climate,* **22,** 6356–6376, doi:10.1175/2009JCLI3020.1.

Hagos, S., and Coauthors, 2010: Estimates of tropical diabatic heating profiles: Commonalities and uncertainties. *J. Climate,* **23,** 542–558, doi:10.1175/2009JCLI3025.1.

Hartmann, D. L., H. H. Hendon, and R. A. Houze Jr., 1984: Some implications of the mesoscale circulations in tropical cloud clusters for large-scale dynamics and climate. *J. Atmos. Sci.,* **41,** 113–121, doi:10.1175/1520-0469(1984)041<0113:SIOTMC>2.0.CO;2.

Houze, R. A., Jr., 1982: Cloud clusters and large-scale vertical motions in the tropics. *J. Meteor. Soc. Japan,* **60,** 396–410.

——, 1989: Observed structure of mesoscale convective systems and implications for large-scale heating. *Quart. J. Roy. Meteor. Soc.,* **115,** 425–461, doi:10.1002/qj.49711548702.

——, 1997: Stratiform precipitation in regions of convection: A meteorological paradox? *Bull. Amer. Meteor. Soc.,* **78,** 2179–2196, doi:10.1175/1520-0477(1997)078<2179:SPIROC>2.0.CO;2.

——, 2004: Mesoscale convective systems. *Rev. Geophys.,* **42,** RG4003, doi:10.1029/2004RG000150.

——, and A. K. Betts, 1981: Convection in GATE. *Rev. Geophys.,* **19,** 541–576, doi:10.1029/RG019i004p00541.

Huffman, G. J., R. F. Adler, M. Morrissey, D. T. Bolvin, S. Curtis, R. Joyce, B. McGavock, and J. Susskind, 2001: Global precipitation at One-Degree Daily resolution from multisatellite observations. *J. Hydrometeor.,* **2,** 36–50, doi:10.1175/1525-7541(2001)002<0036:GPAODD>2.0.CO;2.

Jakob, C., and G. Tselioudis, 2003: Objective identification of cloud regimes in the Tropical Western Pacific. *Geophys. Res. Lett.,* **30,** 2082, doi:10.1029/2003GL018367.

——, and C. Schumacher, 2008: Precipitation and latent heating characteristics of the major tropical western Pacific cloud regimes. *J. Climate,* **21,** 4348–4364, doi:10.1175/2008JCLI2122.1.

Jiang, X., and Coauthors, 2011: Vertical diabatic heating structure of the MJO: Intercomparison between recent reanalyses and TRMM estimates. *Mon. Wea. Rev.,* **139,** 3208–3223, doi:10.1175/2011MWR3636.1.

Kodama, Y.-M., M. Katsumata, S. Mori, S. Satoh, Y. Hirose, and H. Ueda, 2009: Climatology of warm rain and associated latent heating derived from TRMM-PR observations. *J. Climate,* **22,** 4908–4929, doi:10.1175/2009JCLI2575.1.

L'Ecuyer, T. S., and G. L. Stephens, 2003: The tropical oceanic energy budget from the TRMM perspective. Part I: Algorithm and uncertainties. *J. Climate,* **16,** 1967–1985, doi:10.1175/1520-0442(2003)016<1967:TTOEBF>2.0.CO;2.

——, and ——, 2007: The tropical atmospheric energy budget from the TRMM perspective. Part II: Evaluating GCM representations of the sensitivity of regional energy and water cycles to the 1998–99 ENSO cycle. *J. Climate,* **20,** 4548–4571, doi:10.1175/JCLI4207.1.

——, and G. McGarragh, 2010: A 10-year climatology of tropical radiative heating and its vertical structure from TRMM observations. *J. Climate,* **23,** 519–541, doi:10.1175/2009JCLI3018.1.

Lindzen, R. S., and S. Nigam, 1987: On the role of sea surface temperature gradients in forcing low-level winds and convergence in the tropics. *J. Atmos. Sci.,* **44,** 2418–2436, doi:10.1175/1520-0469(1987)044<2418:OTROSS>2.0.CO;2.

Ling, J., and C. Zhang, 2011: Structural evolution in heating profiles of the MJO in global reanalyses and TRMM retrievals. *J. Climate,* **24,** 825–842, doi:10.1175/2010JCLI3826.1.

Lungu, T., Ed., 2006: QuikSCAT science data product user's manual, version 3.0. NASA Tech. Rep. D-18053-RevA, 91 pp.

Machado, L. A. T., and W. B. Rossow, 1993: Structural characteristics and radiative properties of tropical cloud clusters. *Mon. Wea. Rev.,* **121,** 3234–3260, doi:10.1175/1520-0493(1993)121<3234:SCARPO>2.0.CO;2.

Mapes, B. E., and R. A. Houze Jr., 1995: Diabatic divergence profiles in western Pacific mesoscale convective systems. *J. Atmos. Sci.,* **52,** 1807–1828, doi:10.1175/1520-0469(1995)052<1807:DDPIWP>2.0.CO;2.

Masunaga, H., and T. S. L'Ecuyer, 2014: A mechanism of tropical convection inferred from observed variability in the moist static energy budget. *J. Atmos. Sci.,* doi:10.1175/JAS-D-14-0015.1, in press.

Matsuno, T., 1966: Quasi-geostrophic motions in the equatorial area. *J. Meteor. Soc. Japan,* **44,** 25–43.

Milliff, R. F., J. Morzel, D. B. Chelton, and M. H. Freilich, 2004: Wind stress curl and wind stress divergence biases from rain effects on QSCAT surface wind retrievals. *J. Atmos. Oceanic Technol.,* **21,** 1216–1231, doi:10.1175/1520-0426(2004)021<1216:WSCAWS>2.0.CO;2.

Neelin, J. D., and I. M. Held, 1987: Modeling tropical convergence based on the moist static energy budget. *Mon. Wea. Rev.,* **115,** 3–12, doi:10.1175/1520-0493(1987)115<0003:MTCBOT>2.0.CO;2.

North, G. R., T. L. Bell, R. F. Cahalan, and F. J. Moeng, 1982: Sampling errors in the estimation of empirical orthogonal functions. *Mon. Wea. Rev.,* **110,** 699–706, doi:10.1175/1520-0493(1982)110<0699:SEITEO>2.0.CO;2.

Raymond, D. J., S. L. Sessions, A. H. Sobel, and Ž. Fuchs, 2009: The mechanics of gross moist stability. *J. Adv. Model. Earth Syst.,* **1,** 9, doi:10.3894/JAMES.2009.1.9.

Rossow, W., and R. Schiffer, 1999: Advances in understanding clouds from ISCCP. *Bull. Amer. Meteor. Soc.,* **80,** 2261–2287, doi:10.1175/1520-0477(1999)080<2261:AIUCFI>2.0.CO;2.

——, G. Tselioudis, A. Polak, and C. Jakob, 2005: Tropical climate described as a distribution of weather states indicated by distinct mesoscale cloud property mixtures. *Geophys. Res. Lett.,* **32,** L21812, doi:10.1029/2005GL024584.

——, A. Mekonnen, C. Pearl, and W. Goncalves, 2013: Tropical precipitation extremes. *J. Climate,* **26,** 1457–1466, doi:10.1175/JCLI-D-11-00725.1.

Schumacher, C., R. A. Houze Jr., and I. Kraucunas, 2004: The tropical dynamical response to latent heating estimates derived from the TRMM precipitation radar. *J. Atmos. Sci.,* **61,** 1341–1358, doi:10.1175/1520-0469(2004)061<1341:TTDRTL>2.0.CO;2.

Sherwood, S. C., S. Bony, and J.-L. Dufresne, 2014: Spread in model climate sensitivity traced to atmospheric convective mixing. *Nature,* **505,** 37–42, doi:10.1038/nature12829.

Shige, S., Y. N. Takayabu, W.-K. Tao, and D. E. Johnson, 2004: Spectral retrieval of latent heating profiles from TRMM PR data. Part I: Development of a model-based algorithm. *J. Appl. Meteor.,* **43,** 1095–1113, doi:10.1175/1520-0450(2004)043<1095:SROLHP>2.0.CO;2.

——, ——, ——, and C.-L. Shie, 2007: Spectral retrieval of latent heating profiles from TRMM PR data. Part II: Algorithm improvement and heating estimates over tropical ocean regions. *J. Appl. Meteor. Climatol.,* **46,** 1098–1124, doi:10.1175/JAM2510.1.

——, ——, and ——, 2008: Spectral retrieval of latent heating profiles from TRMM PR data. Part III: Estimating apparent moisture sink profiles over tropical oceans. *J. Appl. Meteor. Climatol.,* **47,** 620–640, doi:10.1175/2007JAMC1738.1.

——, ——, S. Kida, W.-K. Tao, X. Zeng, C. Yokoyama, and T. L'Ecuyer, 2009: Spectral retrieval of latent heating profiles from TRMM PR data. Part IV: Comparisons of lookup tables from two- and three-dimensional cloud-resolving model simulations. *J. Climate,* **22,** 5577–5594, doi:10.1175/2009JCLI2919.1.

Sobel, A. H., and C. S. Bretherton, 2000: Modeling tropical precipitation in a single column. *J. Climate,* **13,** 4378–4392, doi:10.1175/1520-0442(2000)013<4378:MTPIAS>2.0.CO;2.

Stachnik, J. P., 2013: Observed characteristics of clouds and precipitating systems associated with the tropical circulation in global models and reanalyses. Ph.D. dissertation, Texas A&M University, 200 pp.

Stevens, D., A. Ackerman, and C. Bretherton, 2002: Effects of domain size and numerical resolution on the simulation of shallow cumulus convection. *J. Atmos. Sci.,* **59,** 3285–3301, doi:10.1175/1520-0469(2002)059<3285:EODSAN>2.0.CO;2.

Tao, W.-K., S. Lang, J. Simpson, and R. Adler, 1993: Retrieval algorithms for estimating the vertical profiles of latent heat release: Their applications for TRMM. *J. Meteor. Soc. Japan,* **71,** 685–700.

——, and Coauthors, 2001: Retrieved vertical profiles of latent heat release using TRMM rainfall products for February 1998. *J. Appl. Meteor.,* **40,** 957–982, doi:10.1175/1520-0450(2001)040<0957:RVPOLH>2.0.CO;2.

——, and Coauthors, 2006: Retrieval of latent heating from TRMM measurements. *Bull. Amer. Meteor. Soc.,* **87,** 1555–1572, doi:10.1175/BAMS-87-11-1555.

Trenberth, K. E., D. P. Stepaniak, and J. M. Caron, 2000: The global monsoon as seen through the divergent atmospheric circulation. *J. Climate,* **13,** 3969–3993, doi:10.1175/1520-0442(2000)013<3969:TGMAST>2.0.CO;2.

Tselioudis, G., W. Rossow, Y.-C. Zhang, and D. Konsta, 2013: Global weather state and their properties from passive and active satellite cloud retrievals. *J. Climate,* **26,** 7734–7746, doi:10.1175/JCLI-D-13-00024.1.

Webster, P. J., and R. Lukas, 1992: TOGA COARE: The Coupled Ocean–Atmosphere Response Experiment. *Bull. Amer. Meteor. Soc.,* **73,** 1377–1416, doi:10.1175/1520-0477(1992)073<1377:TCTCOR>2.0.CO;2.

Wu, Z., E. S. Sarachik, and D. S. Battisti, 2000: Vertical structure of convective heating and the three-dimensional structure of the forced circulation on an equatorial beta plane. *J. Atmos. Sci.,* **57,** 2169–2187, doi:10.1175/1520-0469(2000)057<2169:VSOCHA>2.0.CO;2.

Yanai, M., S. Esbensen, and J. Chu, 1973: Determination of bulk properties of tropical cloud clusters from large-scale heat and moisture budgets. *J. Atmos. Sci.,* **30,** 611–627, doi:10.1175/1520-0469(1973)030<0611:DOBPOT>2.0.CO;2.

Yu, J.-Y., C. Chou, and J. D. Neelin, 1998: Estimating the gross moist stability of the tropical atmosphere. *J. Atmos. Sci.,* **55,** 1354–1372, doi:10.1175/1520-0469(1998)055<1354:ETGMSO>2.0.CO;2.

Zhang, C., M. McGauley, and N. A. Bond, 2004: Shallow meridional circulation in the tropical eastern Pacific. *J. Climate,* **17,** 133–139, doi:10.1175/1520-0442(2004)017<0133:SMCITT>2.0.CO;2.

——, and Coauthors, 2010: MJO signals in latent heating: Results from TRMM retrievals. *J. Atmos. Sci.,* **67,** 3488–3508, doi:10.1175/2010JAS3398.1.

Zipser, E. J., 1977: Mesoscale and convective-scale downdrafts as distinct components of squall-line structure. *Mon. Wea. Rev.,* **105,** 1568–1589, doi:10.1175/1520-0493(1977)105<1568:MACDAD>2.0.CO;2.

Zuluaga, M. D., C. D. Hoyos, and P. J. Webster, 2010: Spatial and temporal distribution of latent heating in the South Asian monsoon region. *J. Climate,* **23,** 2010–2029, doi:10.1175/2009JCLI3026.1.